

Helical Jet in the Gravitationally Lensed Blazar PKS1830-211

S. Nair¹, C. Jin² & M. A. Garrett³

¹ *Astronomy & Astrophysics Group, Raman Research Institute, C. V. Raman Avenue, Bangalore 560080, India*

² *National Astronomical Observatories, Chinese Academy of Sciences, A20 Datun Road, Chaoyang District, Beijing 100012, China*

³ *Joint Institute for VLBI in Europe, NFRA, 7990 AA Dwingeloo, The Netherlands*

Accepted: June 27, 2005 Received: May 6, 2005 In original form: March 11, 2005

ABSTRACT

Recent radio VLBI observations of the complex gravitationally lensed system PKS1830-211 have thrown up some questions with regard to the processes occurring at the heart of the blazar source at a redshift of 2.51, which is viewed almost straight down the jet axis. This work links, by a model of a helical jet tracked by ballistically ejected plasmons from a precessing nozzle, observations on the scale of tens of microarcseconds to those on the scale of milliarcseconds. An observed jet precession period of 1.08 years is inferred from the model, translating to an intrinsic period of 30.8 years for a source at redshift $z_s = 2.51$ and an assumed jet bulk velocity β of $0.99c$. This fits well with the picture of the active galactic nucleus hosting a binary black hole system at its centre, with the jet emitted by one member of the system, and the precession as being due to its orbital motion around its companion.

Key words: gravitational lensing: individual: PKS1830-211 — galaxies: active— BL Lacertae objects: individual: PKS1830-211

1 INTRODUCTION

The much-studied gravitationally lensed system, PKS1830-211, was identified as such by Rao & Subrahmanyam (1988), and is one of the strongest radio sources in the sky at centimetric wavelengths. On arcsecond scale, it consists of two prominent radio core-knot structures, lensed images of each other, each core-knot axis being roughly perpendicular to the line of separation of the two cores (the two cores being separated by about $0''.98$ and aligned roughly northeast (NE) and southwest (SW) in the plane of the sky). The two core-knot groups (hereafter NE and SW groups) are point-inversion symmetric with respect to the centre of the system, and show somewhat weaker diffuse emission (Rao & Subrahmanyam 1988, Subrahmanyam et al. 1990); in the radio L-band, the diffuse emission is extended enough that its images actually close round, linking the image groups and making a pseudo-Einstein Ring system (Jauncey et al. 1991), with nearly half of the total flux density of about 12 Jy coming from the cores. The cores themselves have flat radio spectra (Rao & Subrahmanyam 1988). On the scale of milliarcseconds in the radio at 43 GHz, a weaker, inner knot accompanies each of the bright cores, on the same side of each core as the arcsecond-scale knot (which is not detected at this resolution), and separated from it by ~ 1 mas (Gar-

rett et al 1997, Jones et al., Guirado et al. 1999, Jin et al. 2003).

Jin et al. (2003) infer that there are time-dependent positional variations in the radio centroids of emission in the bright cores at 43 GHz, resulting in changes in the separation of the two core components on the scale of 10's to 100's μs (Figure 1) between successive observational epochs. Significant radio variability has been reported (Lovell et al. 1996, van Ommen et al. 1995, Hagiwara et al. 1996 and Lovell et al. 1998); in fact, Lovell et al. (1998) report a time delay between the arrival time at the observer of variations in one core image relative to (correlated) variations in the other, of 26_{-5}^{+4} days. However, Romero et al. (1997) report this system to be non-variable, based on data taken during 1995-1996 in the radio L-band. Lovell et al's (1998) analysis was based on 8.6 GHz data between 1996 and 1997, during which period dramatic variations occurred.

The source has been identified in EGRET observations (Mattox et al., 1997).

In the X-ray, ROSAT observations have revealed absorption against the compact images, in excess of what may be reasonably attributed to our Galaxy, implicating a foreground (lensing) galaxy (Mathur & Nair 1997). ASCA observations (Oshima et al. 2001) suggest significant X-ray variability in the system, so that the ratio of the NE image's

emission to that of the SW image was a factor of 7 (as compared with a typical factor of 1 to 1.8 in the radio). Given that the source properties resemble those of a blazar, this is very likely a variation intrinsic to the blazar rather than a lens-induced one, though observations of correlated spectral hardness changes would be necessary to confirm that such a phenomenon indeed occurs in this system.

The system that acts as the gravitational lens, now known to be fairly complex, is believed to be in the main a gas-rich massive spiral galaxy, with a measured redshift of $z_1 = 0.89$, through molecular absorption line studies (Wiklind & Combes 1996, Carilli et al. 1998, Chengalur et al. 1999). In the optical, observations are hindered by the location of the system (in Galactic coordinates, $l = 12^\circ.2$, $b = -5^\circ.7$; here optical extinction is experienced of order 2.7 magnitudes, *cf.* Subrahmanyan et al 1990); nonetheless Frye et al. (1999) (I and K band observations), Courbin et al. (1998, 2002) (V, I, J, H & K bands), Lehar et al. (2000) (H and I bands) and Winn et al. (2002) (I and V bands) have presented a wealth of optical and near-IR data, which, suitably image processed, reveal a spiral galaxy lens seen almost face on, with possibly a secondary lens nearby, and perhaps some sign of a lower redshift spiral galaxy about $2''.5$ southwards of the system. Lidman et al. (1999) determine through infrared spectroscopy a redshift for the source ($z_s = 2.51$). HI observations (Lovell et al. 1996) have earlier revealed some absorption at redshift $z_2 = 0.19$. The presence in the optical and IR bands of a foreground low redshift spiral galaxy is highly suggestive of the existence of a secondary lens.

Gravitational lens modeling of the system that has attempted to reproduce a range of image properties (Subrahmanyan et al. 1990, Kochanek & Narayan 1992, Nair et al. 1993), has shown the system to be consistent with an isolated elliptical lens of mass of the order of that of a spiral galaxy. However, in view of the apparently complex optical/IR structure subsequently observed along the foreground and upto the lens redshift, a detailed remodeling is in order.

The present work seeks to provide an explanation for the puzzling observations of Garrett et al. (1998) and Jin et al. (2003), wherein it is shown that structural and temporal variations occur in and around the radio core images in this system in VLBA observations at 43 GHz. These observations probe the system at the highest resolution to date, of considerable interest because of the combination of a high redshift source ($z_s = 2.5$) and enhanced resolution due to magnification by lensing. For the purpose of the present study, a full reworking of the lens model is actually inessential; instead, certain lens properties applicable to this system will be either invoked or derived as required.

2 SOME PROPERTIES OF THE LENS

Considering the optical and infrared observations of possible multiple lensing bodies along the line of sight to the system (as described in the previous section), only the most elementary assumptions regarding the lens system will be made. At the location of each image in the plane of the sky, it is assumed that it is possible to define a 2×2 source-to-image coordinate transformation matrix that is symmetric. This is valid provided one or the other of two circumstances

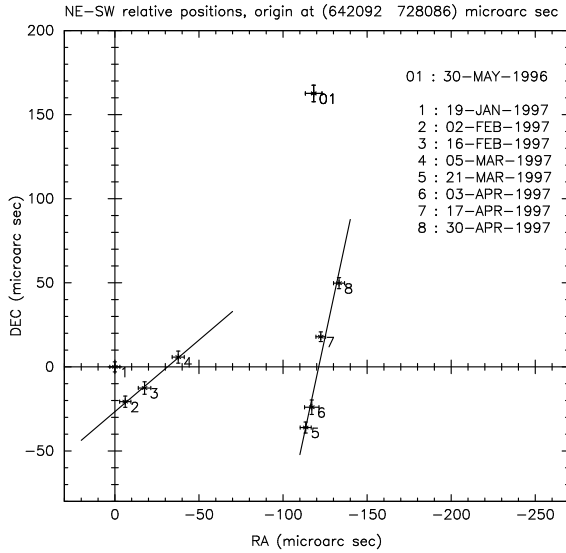
occurs: (a) the dominant lensing agents are roughly at the same distance from the observer, or from the source, so that they can be said to inhabit the same lens plane (*cf.* Blandford & Narayan 1986), or (b) save for the main deflectors in the same lens plane, lenses at other redshifts provide only a shear perturbation (however strong or weak) to the main lens's action. Then the lensing equations reduce to one identical with single-plane lensing, and source-to-image transformation matrices are symmetric as a result (Kovner 1987). The latter assumption is adopted in view of the possible existence of a lens at $z = 0.19$, which is seen $2''.5$ south, in the plane of the sky, of the lensed images in the system. In fact, since it has proven fairly successful to model this system with a single elliptical lens (Subrahmanyan et al. 1990, Kochanek & Narayan 1992, Nair et al. 1993), it is possible that the main lens, a spiral galaxy at $z_1 = 0.89$ which is viewed almost face-on, is aided by shear roughly along the north-south direction by the foreground lens, mimicking the behaviour of a single elliptical lens with such an orientation (note that this is close to the direction of the major axis of the elliptical lens model in Nair et al. 1993). That the effect of the foreground ($z_2 = 0.19$) lens can be treated as a perturbation on the main lens' action derives some support from the fact that lens models place the effective lens centre between the NE and SW groups of images, and somewhat closer to the negative-parity SW group of images (the parity of which is demonstrated by the fact that temporal variations in its core's radio flux density lag behind those in the NE core; *cf.* Lovell et al. 1998). This would be as expected for a single lensing galaxy, suggesting that the actual lens is not very far from one.

3 A LENSED HELICAL JET

3.1 Inferred source evolution from observations on the scale of tens of microarcseconds

Figure 1 (from Fig.3 of Jin et al. 2003), plots, for 8 successive epochs of VLBA observations at 43 GHz ($0''.3$ mas FWHM beam), changes in declination versus changes in right ascension (RA) of the position vector from the centroid of emission of the NE image core to that of the SW image core, all relative to the first epoch (t_{ref}) of observation. Formally, the error in estimating these changes is of the order of $3 \mu\text{as}$ as both the core images appear in the same field of view in each observation (Jin et al. 2003). The plot is displayed here with straight-line fits to two remarkably linear tracks that can be identified in the plot. In this section, an explanation for this phenomenon will be sought.

Anticipating a physical model to be discussed later in this section, it is assumed that the source, a blazar, emits plasmons, one by one, from its central engine, and that the observed (but essentially unresolved) core radio emission is dominated for a while by that of the most recently emitted plasmon, which propagates away from the central engine with constant velocity before fading from view (its spectral evolution, synchrotron self-absorbed, being as described in, for example, van der Laan 1966). Any changes in the location of the radio emission of the central engine itself are assumed to be undetectable as a function of time ($\leq 3 \mu\text{as}$). (The actual position of the central engine then drops out of


Figure 1.

Changes in the centroids of radio emission in the NE and SW cores; their separations as a function of epoch relative to Epoch 1 in the figure (from Fig.3 of Jin et al. 2003). Superposed are straight line fits to the two linear runs apparent in the data, which yield slopes of (for epochs 2-3-4) 0.85 ± 0.07 and (for epochs 5-6-7-8), 4.66 ± 0.48 .

the following computations, because we consider changes in position relative to a reference epoch).

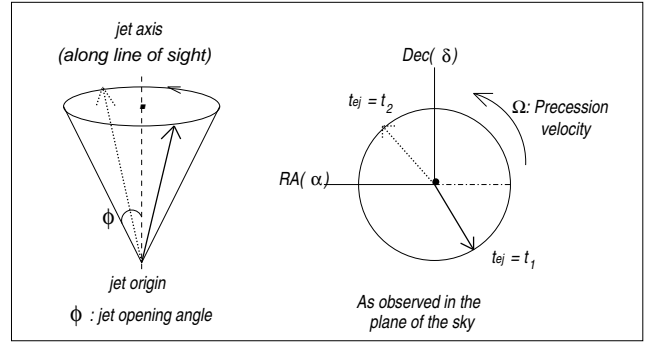
The radio core of the source and its associated features are lensed into two images, denoted by the subscripts A (the NE group) and B (the SW group) in what follows. Changes occurring in the unlensed source shall be referred to as being in the *source plane*, and the corresponding effects in the images shall be referred to as occurring in the *image plane*. For the unlensed source, let the angular distance of an ejected plasmon from the central engine at any given epoch of observation, t_k , be denoted by $\Delta\Phi[t_k]$, its components along the directions of increasing RA and declination being represented by $\Delta\Phi_\alpha$ and $\Delta\Phi_\delta$ respectively.

Now, local to a point in a gravitationally lensed image, positional changes are mapped through a linear transformation of the underlying changes in the source. That is, for small changes $\Delta\Phi$ in the source, the corresponding changes in images A and B are given by:

$$(\Delta\Phi_{\alpha,A}, \Delta\Phi_{\delta,A}) = \begin{pmatrix} a_1 & p \\ p & a_4 \end{pmatrix} \begin{pmatrix} \Delta\Phi_\alpha \\ \Delta\Phi_\delta \end{pmatrix} \quad (1)$$

$$(\Delta\Phi_{\alpha,B}, \Delta\Phi_{\delta,B}) = \begin{pmatrix} b_1 & q \\ q & b_4 \end{pmatrix} \begin{pmatrix} \Delta\Phi_\alpha \\ \Delta\Phi_\delta \end{pmatrix} \quad (2)$$

Two comments are in order at this point: (a) It has been assumed that the source-to-image transformation matrices are symmetric, under the circumstances discussed in Section 2 and (b), when considering observed changes in the images, it is necessary to account for the fact that events in the SW image are behind those in the NE image, by an amount equal to the time delay between the images, $\tau = 26^{+5}_{-4}$ days (Lovell et al. 1998). Thus the observed changes in the two images map back to two different epochs in the source itself


Figure 2.

Underlying model for the precessing jet. The jet emission vector makes an angle ϕ (jet half-opening angle) with its axis, which is also the line of sight by assumption (*left*). From time to time, plasmons are ejected, and each propagates with constant velocity along the surface of the cone defined by the motion of the emission vector. (*Right*): The view along the line of sight to the blazar, prior to lensing.

(epochs referring to events in the source will hereinafter be called *source epochs*, as distinct from *observer epochs*).

Formally, it is possible to define a relative or image-to-image transformation matrix (in this case, the SW image-to-NE image, or ‘SW2NE’, matrix will be defined):

$$(\Delta\Phi_{\alpha,A}, \Delta\Phi_{\delta,A}) = \begin{pmatrix} T_1 & T_2 \\ T_3 & T_4 \end{pmatrix} \begin{pmatrix} \Delta\Phi_{\alpha,B} \\ \Delta\Phi_{\delta,B} \end{pmatrix}, \quad (3)$$

where $\eta = (b_1b_4 - q^2)$, $T_1 = (a_1b_4 - pq)/\eta$, $T_2 = (b_1p - a_1q)/\eta$, $T_3 = (pb_4 - qa_4)/\eta$, and $T_4 = (a_4b_1 - pq)/\eta$. When evaluating this matrix from the observations, which here include evolving components, care must be taken that appropriate corrections are introduced for the differing source epochs (or alternatively, light arrival time delays) corresponding to each of the images.

Adopting the Hjellming & Johnston (1981) model for SS433 (or the Gower et al. 1982 model, as applied to AGNs) for a precessing helical jet, we assume that a plasmon in the jet is ejected from the central engine of the source with constant velocity \bar{v} along the surface of a cone of half-opening angle ϕ , the symmetry axis of which is the axis of the jet (*cf.* Fig.2). New plasmons are ejected ballistically from time to time. The plasmon ejection velocity vector precesses with angular velocity Ω about the cone’s surface, making a constant angle ϕ with the jet axis, so that each subsequent plasmon is ejected at a different phase of the jet’s precession. Once ejected with a given velocity \bar{v} , a plasmon continues to propagate away from the central engine with that velocity (or it fades from view before it appears to decelerate or accelerate). Each plasmon is assumed to consist of an isotropically expanding cloud of synchrotron-emitting electrons, so that the centroid of emission is not affected by its evolution. As mentioned earlier, it is assumed that only one plasmon at a time dominates the unresolved radio emission from the radio core. It is also assumed that the line of sight of the observer coincides with the jet precession axis, for simplicity of calculations.

Let a plasmon be ejected from the central engine of the source. The observable proper motion of the unlensed plasmon from the time of its ejection, t_{ej} , to the epoch, k ,

of observation, t_k , would be given by its components in the plane of the sky:

$$\Delta\Phi_\alpha = \frac{v_\alpha(t_k - t_{ej})}{d(1 - v_x/c)} \quad (4)$$

$$\Delta\Phi_\delta = \frac{v_\delta(t_k - t_{ej})}{d(1 - v_x/c)} \quad (5)$$

Here d is the angular diameter distance to the source, and c is the velocity of light. The source time interval ($t_k - t_{ej}$) is corrected for the motion of the plasmon at relativistic speeds along the line of sight during its propagation. (To convert a source time interval itself to the observed time interval, $(\delta t)_{\text{observer}} = (\delta t)_{\text{source}}/(1 - v_x/c)/(1 + z_s)$, where z_s is the redshift of the source; here one corrects for cosmological effects as well. This term is included in the angular diameter distance in Eqns. 4 & 5 and therefore need not be specified explicitly).

At epoch t_k , we observe in image A:

$$\Delta\Phi_{\alpha,A} [t_k] = a_1 \Delta\Phi_\alpha^A + p \Delta\Phi_\delta^A$$

$$\Delta\Phi_{\delta,A} [t_k] = p \Delta\Phi_\alpha^A + a_4 \Delta\Phi_\delta^A$$

where the superscript ‘A’ is used to indicate that an appropriate correction for the light travel time along the path through image A must be applied. For image B:

$$\Delta\Phi_{\alpha,B} [t_k] = b_1 \Delta\Phi_\alpha^B + q \Delta\Phi_\delta^B$$

$$\Delta\Phi_{\delta,B} [t_k] = q \Delta\Phi_\alpha^B + b_4 \Delta\Phi_\delta^B$$

with a similar use of superscript as before. The convention that will be used in the following is that for events in image A, $(t_k - t_{ej})$ is written as $(t_k - {}_A t_{ej})$, and for image B, as $(t_k - {}_B t_{ej}) = (t_k - {}_A t_{ej} - \tau)$, explicitly writing the light travel time difference τ between the paths through images A and B into the expressions.

At this point contact is possible with the observations in Figure 1. What is observed in each image is a change $\overline{\Delta\Phi}$ from a location $\bar{\theta} = (\theta_\alpha, \theta_\delta)$, the position of the lensed central engine. It is assumed that $\bar{\theta}$ for each image remains fixed through the different epochs of observation; since the changes in Figure 1 are plotted relative to a reference epoch, the location $\bar{\theta}$ in each image will drop out of all expressions thereafter, hence it will be ignored.

With this simplification, and making the appropriate substitutions, the following quantities are constructed:

$$\begin{aligned} \delta\Phi_\alpha [t_k] &= \Delta\Phi_{\alpha,A} [t_k] - \Delta\Phi_{\alpha,B} [t_k] \\ &= \{(a_1 - b_1)v'_\alpha + (p - q)v'_\delta\}(t_k - {}_A t_{ej}) + \\ &\quad (b_1 v'_\alpha + q v'_\delta)\tau \end{aligned} \quad (6)$$

$$\begin{aligned} \delta\Phi_\delta [t_k] &= \Delta\Phi_{\delta,A} [t_k] - \Delta\Phi_{\delta,B} [t_k] \\ &= \{(p - q)v'_\alpha + (a_4 - b_4)v'_\delta\}(t_k - {}_A t_{ej}) + \\ &\quad (q v'_\alpha + b_4 v'_\delta)\tau \end{aligned} \quad (7)$$

In the above, the prime on quantities v_α and v_δ is used to denote the corresponding velocity components divided by $d(1 - v_x/c)$. Also note the implicit assumption that at the epoch of observation, t_k , the plasmon responsible for the

observations is present in both images (i.e., $t_k \geq {}_A t_{ej} + \tau$). As long as only one plasmon at a time dominates the source emission on this scale of observation, and it expands isotropically (so that the centroid of radio emission is not affected by its evolution), it is possible to neglect the effects of evolution of the plasmon itself over the timescale of observation and deal simply with positional changes of its centroid relative to the core. The presence of a second evolving plasmon coexisting with the first would considerably complicate this simple picture!

The changes plotted in Figure 1 are relative to a reference epoch t_{ref} , so we construct new quantities, which are now the abscissas and ordinates of the plot in Figure 1 :

$$\begin{aligned} \delta(\delta\Phi_\alpha) [t_k] &= \delta\Phi_\alpha [t_k] - \delta\Phi_\alpha [t_{\text{ref}}] \\ &= (a_1 - b_1) v'_\alpha + (p - q) v'_\delta \end{aligned} \quad (8)$$

$$\begin{aligned} \delta(\delta\Phi_\delta) [t_k] &= \delta\Phi_\delta [t_k] - \delta\Phi_\delta [t_{\text{ref}}] \\ &= (p - q) v'_\alpha + (a_4 - b_4) v'_\delta \end{aligned} \quad (9)$$

$$(10)$$

The slope m of a particular linear track in Figure 1 is given by (dropping the primes on v_α and v_δ as unnecessary here):

$$\begin{aligned} m &= \frac{\delta(\delta\Phi_\alpha) [t_k] - \delta(\delta\Phi_\alpha) [t_j]}{\delta(\delta\Phi_\delta) [t_k] - \delta(\delta\Phi_\delta) [t_j]} \\ &= \frac{(a_1 - b_1) v_\alpha + (p - q) v_\delta}{(p - q) v_\alpha + (a_4 - b_4) v_\delta} \end{aligned} \quad (11)$$

$$(12)$$

From the above expressions it is now apparent that the change in slope of the tracks between the run of epochs 2, 3 & 4 (slope $m_1 = 0.85 \pm 0.07$) and that of epochs 5, 6, 7 & 8 (slope $m_2 = 4.66 \pm 0.48$) is effected by a change in the quantities v_α and v_δ , projections of the ejection velocity vector \vec{v} of a plasmon, in the plane of the sky. In the context of our model, this corresponds to the dominance of a new plasmon between epochs 4 & 5, which has been ejected at a phase in the precession of the jet which is distinct from that of the previously ejected plasmon. An obvious question at this point is, what is the actual event that causes a discontinuity between epochs 1 & 2, and again between epochs 4 & 5? The appearance of a new plasmon in the NE image precedes that in the SW image by 26 days, or nearly two successive epochs in our 43 GHz observations, so if the discontinuity were to be caused by its appearance in the NE image, there should be another such discontinuity two epochs later, caused by its manifestation in the SW image. The fact that both linear tracks are more than two epochs long suggests that this is not the case. The reason is somewhat subtle and will be discussed in Section 3.6 after deriving some quantities in connection with the source-to-image transformation matrices, but for the moment we identify the discontinuities in these linear tracks as corresponding to the appearance of new plasmons in the SW image (so that, by the time a discontinuity occurs, the *same* source plasmon is imaged in both the NE and the SW regions).

As an aside, notice that for equal intervals between epochs, the changes $\delta\overline{\delta\Phi}$ should be the same, along a single linear track. That this is only approximately true for each of the two tracks in Figure 1 is an indication that emission near the central core is variable at some level, pulling in or pushing out the centroid of radio emission from time to time.

This results in an apparent change in speed of the emergent plasmon, with no significant change in direction.

For later use, the above expression is recast in a slightly different form:

$$\frac{v_\delta}{v_\alpha} = \frac{\tilde{p}(m - \tilde{a}_1) - (m - \tilde{b}_1)}{\tilde{p}(1 - m\tilde{a}_4) - (1 - m\tilde{b}_4)} \quad (13)$$

where $\tilde{p} = p/q$, $\tilde{a}_1 = a_1/p$, $\tilde{a}_4 = a_4/p$, $\tilde{b}_1 = b_1/q$ and $\tilde{b}_4 = b_4/q$. For a given value of slope m , once the lensing-related quantities \tilde{p} , \tilde{a}_1 , \tilde{a}_4 , \tilde{b}_1 & \tilde{b}_4 are determined, this expression gives the phase of precession of the jet (modulo $n\pi$ radians, where n is a natural number), relative to a suitably chosen reference direction, at the time of ejection of the relevant plasmon. Thus, the difference of the phases between the events slopes m_1 and m_2 , over the known difference in epoch between the observations, yields the angular velocity or rate of precession of the jet's source, $\Omega = \dot{\psi}$:

$$\Omega = \frac{(\psi_2 - \psi_1)}{(t_2 - t_1)}, \quad (14)$$

where:

$$\psi_1 = -Tan^{-1} \left(\frac{v_\delta}{v_\alpha} [m_1] \right) \quad (15)$$

$$\psi_2 = -Tan^{-1} \left(\frac{v_\delta}{v_\alpha} [m_2] \right) \quad (16)$$

and t_1 and t_2 are just the dates of the first epoch of observation of each event (t_1 is epoch 2, 2 Feb 1997, and t_2 is epoch 5, 21 Mar 1997). The uncertainty in the commencement of each event is regarded as being uniformly distributed, between epochs 1 and 2 for t_1 , and between epochs 4 and 5 for t_2 (see Fig. 1).

3.2 The millisecond-scale behaviour

At this point, it is necessary to review some puzzling VLBA observations of PKS1830-211 at 43 GHz which preceded the eight-epoch track of observations of Jin et al. (2003), namely, those of Garrett et al. (1998). These observations revealed dramatic changes in the millisecond scale structure of the two image groups between epochs of observation 30 May 1996 and 14 July 1996. The former epoch of observation showed core-knot structures in both the NE and SW images, as for each of the epochs of observation in Jin et al. (2003), but the latter epoch, quite suddenly and surprisingly, exhibited rich structure in each of the image groups, with as many as six features in the NE image group being potentially identifiable with corresponding features in the SW image group (including the basic core-knot structure, *cf.* Fig. 3). By the time of the beginning of Jin et al.'s (2003) observations (19 January 1997), the system was back to its quiescent phase, with only a simple core-knot structure being imaged. At some point, on a timescale of several weeks to half a year, a dramatic outburst of plasmons occurred, which then evolved and faded from view, and did not recur over the three months that followed, during which Jin et al.'s (2003) monitoring observations of the system were in progress.

It is expected that at least some of the plasmons in the NE image will have corresponding entities in the SW image. Obviously related are features A1 and B1, the core images, and A4 and B4, which are seen in both epochs of observation

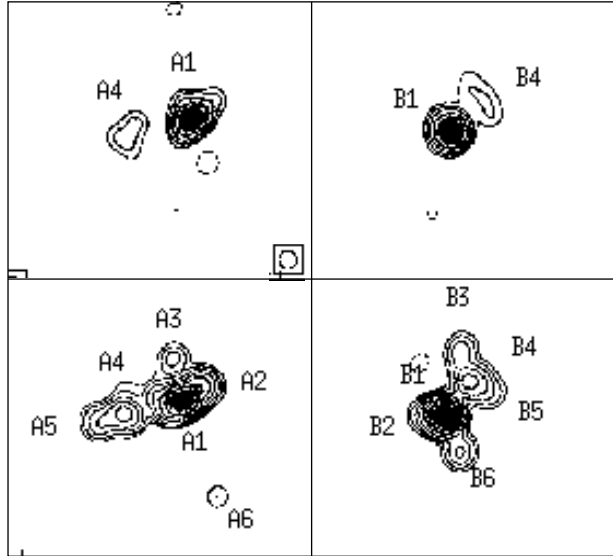


Figure 3.

(Top) : The observations of 30 May 1997 of the NE (left) and SW (right) VLBA images at 43 GHz and 0.33 mas circular restoring beam, showing a simple core-knot structure in each image. (Bottom) : The same as above, but for the next epoch of observations, 14 July 1996, exhibiting rich structure in both images. (Both maps from Garrett et al., 1998.)

in Figure 3 and appear to be static ‘knots’. Of the short-lived features observed in the maps of 14 July 1996, A3 and B3 are obviously not related to each other, from considerations of image parity. However, A2 and B2, A5 and B5, and A6 and B6 are easily seen to be corresponding images, once the effects of the time delay between the NE and SW images (recalling that phenomena in the NE group of images occur about 26 days earlier than they show up in the SW image group), and the distorting effects of lensing in the two image groups are accounted for. It is conjectured at this point that feature A3 has not as yet manifest a counterpart in the SW group of images (it is younger than 26 days), and feature B3 is so aged that its counterpart in the NE group has already evolved below the map detection limits.

3.3 Deriving the relative (SW2NE) image transformation matrix

Assuming that the source-to-image linear transformation matrices remain locally valid across the entire NE or SW image group (on scales of order 1 mas), and that each plasmon in the source is moving ballistically away from the core, on a straight line trajectory, it proves feasible to derive a relative (image-to-image) 2×2 transformation matrix from the observations of 14 July 1996 shown in Figure 3.

Recasting the relative image transformation matrix in the notation of Equation 13,

$$(\Delta\Phi_{\alpha,A}, \Delta\Phi_{\delta,A}) = \begin{pmatrix} T_1 & T_2 \\ T_3 & T_4 \end{pmatrix} \begin{pmatrix} \Delta\Phi_{\alpha,B} \\ \Delta\Phi_{\delta,B} \end{pmatrix}, \quad (17)$$

with $T_1 = \aleph(\tilde{a}_1\tilde{b}_4 - 1)$, $T_2 = \aleph(\tilde{b}_1 - \tilde{a}_1)$, $T_3 = \aleph(\tilde{b}_4 - \tilde{a}_4)$ and $T_4 = \aleph(\tilde{a}_4\tilde{b}_1 - 1)$, and $\aleph = \tilde{p}/(\tilde{b}_1\tilde{b}_4 - 1)$.

For a given feature i , its separation from the core position will be denoted by the vector $(\Delta\Phi_{\alpha,A_i}, \Delta\Phi_{\delta,A_i})$. From the static features, the cores A1 and B1, and knots A4 and B4, one derives the core-knot separation vector in each image group, yielding two constraints (positional coordinates) on the relative transformation matrix (from Eqn. 17):

$$T_1\Delta\Phi_{\alpha,B_4} + T_2\Delta\Phi_{\delta,B_4} - \Delta\Phi_{\alpha,A_4} = 0 \quad (18)$$

$$T_3\Delta\Phi_{\alpha,B_4} + T_4\Delta\Phi_{\delta,B_4} - \Delta\Phi_{\delta,A_4} = 0 \quad (19)$$

The pairs of relationships between A2 and B2, A5 and B5, and A6 and B6 each yield a single constraint, from the shared *direction* of motion of the plasmon in the source (these are evolving features and their actual locations in the NE and SW images refer back to different source times due to the relative time delay). That is, given the location of, say, plasmon B2 in the the SW group relative to its core image B1, the relative transformation matrix must be such that it reproduces the correct direction for plasmon A2 relative to its core A1 in the NE group of images.

For features A2 and B2, A5 and B5, and A6 and B6, the single constraint equation from each pair reads (with $i = 2, 5, 6$):

$$\frac{\Delta\Phi_{\delta,A_i}}{\Delta\Phi_{\alpha,A_i}} = \frac{T_3\Delta\Phi_{\alpha,B_i} + T_4\Delta\Phi_{\delta,B_i}}{T_1\Delta\Phi_{\alpha,B_i} + T_2\Delta\Phi_{\delta,B_i}} \quad (20)$$

which may be rewritten as:

$$\begin{aligned} T_1\Delta\Phi_{\alpha,B_i}\Delta\Phi_{\delta,A_i} + T_2\Delta\Phi_{\delta,A_i}\Delta\Phi_{\delta,B_i} - \\ T_3\Delta\Phi_{\alpha,A_i}\Delta\Phi_{\alpha,B_i} - T_4\Delta\Phi_{\alpha,A_i}\Delta\Phi_{\delta,B_i} = 0 \end{aligned} \quad (21)$$

Thus the observations yield, through Equations 18, 19 and 21, 5 constraint equations for the 4 unknown relative transformation matrix elements, T_j , $j = 1$ to 4. Note that the unknown matrix elements and the observations determining them are implicitly related, non-linear in the observational quantities, and of the form: $\mathbf{F}(\mathbf{X}_a, \mathbf{L}_a) = \mathbf{0}$, where \mathbf{X}_a is the vector of 4 unknowns (matrix elements) and \mathbf{L}_a is the vector of 16 observational quantities. \mathbf{F} itself consists of 5 nonlinear functions. The unknowns in vector \mathbf{X} are solved for via a *mixed adjustment model* (see, for example, A. Leick, 1995), the solution of which is described in the Appendix.

The solution for the elements of the SW2NE transformation matrix are:

$$\mathbf{T}_{SW2NE} = \begin{pmatrix} -1.279 & 0.871 \\ 0.973 & 0.245 \end{pmatrix} \quad (22)$$

Its determinant is: -1.161 . This is the NE/SW image flux density ratio, $k = T_1T_4 - T_2T_3$. The covariance (error) matrix is given by:

$$\mathbf{C}_T = \begin{pmatrix} 0.071 & 0.031 & 0.106 & 0.053 \\ 0.031 & 0.017 & 0.054 & 0.026 \\ 0.106 & 0.054 & 0.342 & 0.165 \\ 0.053 & 0.026 & 0.165 & 0.081 \end{pmatrix} \quad (23)$$

From the expressions immediately following Equation 17, it is possible to express the quantities \tilde{a}_1 , \tilde{a}_4 , \tilde{b}_1 and \tilde{b}_4 in terms of T_1 , T_2 , T_3 and T_4 and \tilde{p} .

$$\tilde{a}_1 = (T_1 - k/\tilde{p})/T_3 \quad (24)$$

$$\tilde{a}_4 = (T_4 - k/\tilde{p})/T_2 \quad (25)$$

$$\tilde{b}_1 = (\tilde{p} - T_4)/T_3 \quad (26)$$

$$\tilde{b}_4 = (\tilde{p} - T_1)/T_2 \quad (27)$$

The evaluation of these quantities depends on the value of \tilde{p} , for which straightforward algebraic methods of determination exist, but which were found to be sensitive to numerical errors of estimate. Hence a different approach has been taken, which will be discussed in Section 3.5.

3.4 The directions of ejection for the milliarcsecond-scale features

It is possible, under the explicit assumption that the source velocity for each evolving plasmon remains constant from the time of generation at least upto the epoch represented by the observations of 14 July 1996 in Figure 3, to relate the distance travelled by a given plasmon as seen in the NE image group of that observation, with the distance that is travelled by its corresponding feature, transformed from the SW group of images via the relative image transformation matrix \mathbf{T}_{SW2NE} and corrected for the lag in time of 26 days for the SW group.

That is, the squared distances are (for $i = 2, 5, 6$):

$$D_{NE}^2 = \Delta\Phi_{\alpha,A_i}^2 + \Delta\Phi_{\delta,A_i}^2, \quad (28)$$

in the NE group of images, and transformed from the SW group to the NE group, are:

$$D_{SW2NE}^2 = (T_1\Delta\Phi_{\alpha,B_i} + T_2\Delta\Phi_{\delta,B_i})^2 + (T_3\Delta\Phi_{\alpha,B_i} + T_4\Delta\Phi_{\delta,B_i})^2 \quad (29)$$

In the NE group, the velocity of motion is $D_{NE}/(t_k - t_{ej})$, and, transformed from the SW group, the corresponding velocity of motion is $D_{SW2NE}/(t_k - t_{ej} - \tau)$, where t_k is the epoch of observation and τ is the time delay between the image groups (assumed to be constant over the span of about a milliarcsecond from the core). If \mathcal{Q} represents the ratio D_{NE}/D_{SW2NE} , then:

$$t_k - t_{ej} = \frac{\tau\mathcal{Q}}{\mathcal{Q} - 1}, \quad (30)$$

with $\mathcal{Q} > 1$.

In order to estimate how well the mixed adjustment model-derived relative transformation matrix actually reproduces the position angles of the features in the NE group of images when it is applied to data from the SW group, the quantities $\Delta\Phi_{\delta,A_i}/\Delta\Phi_{\alpha,A_i}$ (for the original position angle of feature i in the NE group), and $(T_3\Delta\Phi_{\alpha,B_i} + T_4\Delta\Phi_{\delta,B_i})/(T_1\Delta\Phi_{\alpha,B_i} + T_2\Delta\Phi_{\delta,B_i})$ (for the position angle of the transformed data relating to feature i from the SW image) are calculated. For feature A2 (B2), the original position angle is -48° versus a transformed value of -30° but \mathcal{Q} is < 1 (pointing to some inconsistency for this feature); for feature A5 (B5), the original position angle is 104° as compared with a transformed value of 113° , and \mathcal{Q} is 1.272; from Equation 30, a value of 125.2 days is obtained as the ‘age’ of the feature at the time of observation in the NE image on 14 July 1996. For feature A6 (B6), the original position angle is 159° , and the transformed position angle is 158° ; \mathcal{Q} is 6.255 and the ‘age’ of the feature as seen in

the NE image is 30.9 days. (Owing to the existence of significant cross-correlations between quantities derived through the mixed adjustment model – *cf.* Equation 23 – formal errors on quantities derived will be given only for the final result). A cross-check on the mapping of the static knot reveals a perfect match for position. The position angle is 99° in the original; transformed, it is 99° , and as to the distance from the core, it is 0.99 mas in the original and 0.99 mas in the transformed version. Thus the transformation matrix is heavily influenced by feature A6(B6) and the the location of the static knot feature.

Of course, in order to derive the rate of precession of the jet from these numbers, it is necessary to consider the mappings in the source plane of these features, rather than those in the NE image. For this, it is necessary to calculate the velocities of the various evolving features in the source plane. The elements of the source-to-image transformation matrix in Equation 1 can be rewritten, dividing each element by p . Then its inverse reads:

$$\mathbf{T}_{S2NE}^{-1} = p^{-2}(\tilde{a}_1\tilde{a}_4 - 1)^{-2} \begin{pmatrix} \tilde{a}_4 & -1 \\ -1 & \tilde{a}_1 \end{pmatrix} \quad (31)$$

Similarly, for Equation 2, the matrix can be recast and inverted to yield:

$$\mathbf{T}_{S2SW}^{-1} = q^{-2}(\tilde{b}_1\tilde{b}_4 - 1)^{-2} \begin{pmatrix} \tilde{b}_4 & -1 \\ -1 & \tilde{b}_1 \end{pmatrix} \quad (32)$$

Taking the time-derivative (denoted by a superscribed dot) of the angular separations involved, so that one is now dealing with velocities,

$$\dot{\Delta}\Phi_\alpha = p^{-1}(\tilde{a}_1\tilde{a}_4 - 1)^{-1} (\tilde{a}_4\dot{\Delta}\Phi_{\alpha,A} - \dot{\Delta}\Phi_{\delta,A}) \quad (33)$$

$$= q^{-1}(\tilde{b}_1\tilde{b}_4 - 1)^{-1} (\tilde{b}_4\dot{\Delta}\Phi_{\alpha,B} - \dot{\Delta}\Phi_{\delta,B}) \quad (34)$$

$$\dot{\Delta}\Phi_\delta = p^{-1}(\tilde{a}_1\tilde{a}_4 - 1)^{-1} (\tilde{a}_1\dot{\Delta}\Phi_{\delta,A} - \dot{\Delta}\Phi_{\alpha,A}) \quad (35)$$

$$= q^{-1}(\tilde{b}_1\tilde{b}_4 - 1)^{-1} (\tilde{b}_1\dot{\Delta}\Phi_{\delta,B} - \dot{\Delta}\Phi_{\alpha,B}) \quad (36)$$

Now, from the inverse of the image-to-image transformation matrix,

$$\dot{\Delta}\Phi_{\alpha,B} = k^{-1}(T_4\dot{\Delta}\Phi_{\alpha,A} - T_2\dot{\Delta}\Phi_{\delta,A}) \quad (37)$$

$$\dot{\Delta}\Phi_{\delta,B} = k^{-1}(T_1\dot{\Delta}\Phi_{\delta,A} - T_3\dot{\Delta}\Phi_{\alpha,A}) \quad (38)$$

so that, substituting for \tilde{a}_1 and \tilde{a}_4 , or \tilde{b}_1 and \tilde{b}_4 from Equations 24 to 27 and with a little algebra, one obtains:

$$\frac{\dot{\Delta}\Phi_\delta}{\dot{\Delta}\Phi_\alpha} = \frac{T_2}{T_3} \frac{(\tilde{p}\dot{\Delta}\Phi_{\delta,B} - \dot{\Delta}\Phi_{\delta,A})}{(\tilde{p}\dot{\Delta}\Phi_{\alpha,B} - \dot{\Delta}\Phi_{\alpha,A})} = \frac{v_\delta}{v_\alpha} \quad (39)$$

This expression yields (as in the microarcsecond-scale analysis discussed earlier) the phase (modulo $n\pi$) of ejection of the relevant plasmon, with a suitable choice of reference direction. The quantities $\dot{\Delta}\Phi_{\alpha,B}$ and $\dot{\Delta}\Phi_{\delta,B}$ are obtained from $\dot{\Delta}\Phi_{\alpha,B}$ and $\dot{\Delta}\Phi_{\delta,B}$ by dividing by $(t_k - t_{ej} - \tau)$, and $\dot{\Delta}\Phi_{\alpha,A}$ and $\dot{\Delta}\Phi_{\delta,A}$ are obtained by dividing $\dot{\Delta}\Phi_{\alpha,A}$ and $\dot{\Delta}\Phi_{\delta,A}$ by $(t_k - t_{ej})$. To estimate the rate of precession of the jet from expression 39, the phases of ejection, ψ_j , are calculated for plasmons j (with $j = 5, 6$) and the observed time that has lapsed between the ejection of plasmon 5 and plasmon 6 is calculated as $(t_k - t_{ej,6}) - (t_k - t_{ej,5})$, where t_k , the shared epoch of observation, drops out of the estimate. The rest of the calculation follows along the lines described for the microarcsecond scale analysis.

3.5 Evaluating the period of precession of the jet from milliarcsecond and microarcsecond scale information

Expressions 13 and 39 are, respectively, the phases of ejection of various plasmons on the microarcsecond and milliarcsecond scales, as derived from observables. Note that both expressions require the evaluation of \tilde{p} . In order to do this, it will be assumed that the period of precession of the relativistic jet remains the same when evaluated from data on the scale of tens of microarcseconds, as from data on the scale of milliarseconds (for a jet opening half-angle of, say, $0^\circ.5$ and assuming a typical linear magnification by the gravitational lens by a factor of 3, this difference of scale corresponds to source-intrinsic times of order 10^3 years, too short to expect a significant evolution in the precession velocity of the jet). Hence a range of values of \tilde{p} is considered, and its actual value is determined from the coincidence on these two scales of calculated values of the rate of precession of the jet, which exercise also determines the rate of precession itself.

The rate of precession is evaluated as that which would have been observed in the absence of the lens, rather than that intrinsic to the source, since the component of the bulk velocity of the jet along the line of sight cannot be determined (but is expected to be close to the velocity of light). It is calculated as described in Sections 3.1 and 3.4, over a range of values $\tilde{p} = p/q$. Recalling that the actual phases of ejection are only determined modulo $n\pi$, there is a degeneracy in determining the difference of phases $\psi_2 - \psi_1$ for both the milliarcsecond and the microarcsecond analyses. This means that each separation $\psi_i - \psi_j$ actually corresponds to four possible branches. Each of these branches is plotted against \tilde{p} in Figure 4. At this point, it is apparent that a value of \tilde{p} of ~ 0.3 , and a precession rate of 0.016 radians/day (corresponding to an observed period of 1.08 years) permit a coincidence of the milliarcsecond and microarcsecond scale results, so these values are adopted. To obtain the intrinsic source rotation period, the observed period must be corrected for the cosmological time dilation on account of the source being at a redshift of 2.5, and for the change in time interval on account of the jet velocity in the source. The first correction reduces the period by a factor of 3.5, and the second increases it by a factor of $1/(1 - \beta_{los})$, where $\beta_{los} = v_x/c$, with c as the velocity of light. For small jet opening angles, $\beta_{los} \sim v_{jet}/c$. Assuming a value of $\beta = 0.99$, the intrinsic period is calculated to be 30.8 years.

Deriving a period of 1.08 years from the observations raises a question about the authenticity of the results obtained in this paper. We have checked carefully for the possibility of effects related to the annual motion of the Earth around the Sun. The paper of Jin et al. (2003), from which the microarcsecond scale observations are drawn, included a correction for the differential annual aberration between the NE and SW groups of images (separated by ~ 1 arcsec), which is typically of the order of tens of microarcseconds. Relative annual parallax between the NE and SW core images is of order 10^{-4} μas , too small to produce a spurious effect in the observations. (As an aside, another possible source of lensing capable of causing a differential shift in the location of the NE core image relative to the SW one is the Sun itself, which was always more than 15 degrees away from PKS1830-211 in the observations of Jin et al. (2003), thus

producing a differential shift in the NE core image relative to the SW core image of much less than a microarcsecond). Another reason that we do not consider our present result to be a consequence of the Earth's motion around the Sun is the coincidence of this result as obtained from the milliarcsecond scale data of Garrett et al. (1998) with that obtained from the microarcsecond scale data of Jin et al. (2003), as shown in Figure 4. It is difficult to see how the annual motion of the Earth could arrange for this, especially as the milliarcsecond scale data is just one actual epoch of observation (which effectively includes two epochs for the source only because of the existence of two groups of lensed images mapping back to source events separated in time by the time delay of 26 days).

The error in evaluating the precession period is estimated via a Monte Carlo exercise that generates, for each of 60,000 experiments, a random selection of all the observational errors, taking into account the cross-correlations between elements of the SW2NE image-to-image transformation matrix, and then computes the desired precession rate for a value of $\tilde{p} = p/q$ of 0.3. For the microarcsecond scale analysis, the precession rate (in radians per day with $1 - \sigma$ errors) is 0.0155 ($-0.0166, 0.0415$), and for the milliarcsecond scale analysis, the corresponding values are 0.0164 ($-0.575, 0.987$). The large errors on the milliarcsecond scale result are mainly due to the form of the expression used to evaluate the times of ejection for the two plasmons (see Eqn. 30).

The foregoing results are derived, as mentioned earlier, for an assumed perfect alignment of the line of sight with the jet axis. Typically, this is not the case, although it is expected that the alignment of the two is to within a few degrees for blazar sources. The effect of considering an inclination of the jet axis to the line of sight can be estimated from expressions (1), (2) and (3) for the x , y and z velocity components of a plasmon in the precessing jet model of Gower et al. (1982), where axes z and y are in the plane of the sky and centred on the central engine, and axis x is along the line of sight. In general, an additional rotation through an angle χ of Gower et al.'s y and z axes about the x axis is necessary to bring the model into alignment with the right ascension and declination axes. Let the jet half-opening angle be ϕ , and let, as in earlier expressions, the angle through which the jet has precessed at the time of observation, as measured from a reference time t_{ref} , be ψ . Then, with i as the inclination angle of the jet axis to the line of sight, the inferred value of v_s/v_α from, *e.g.*, Equation 39, is related to the precession angle ψ (for each plasmon considered) by:

$$\frac{\sin\chi + \left(\frac{v_s}{v_\alpha}\right)\cos\chi}{\cos\chi - \left(\frac{v_s}{v_\alpha}\right)\sin\chi} = \frac{\sin\phi\sin\psi}{\sin(i)\cos\phi - \cos(i)\sin\phi\cos\psi} \quad (40)$$

From the milliarcsecond scale data, for example, with a jet inclination angle of 0° , for feature 5, $\psi = 200^\circ$, and $t_{ej} - t_{ref} = 125.2$ days, and for feature 6, the corresponding values are -69° and 30.9 days, yielding, as mentioned above, a precession period intrinsic to the source of 30.8 years. For non-zero values of i and ϕ , in order to obtain the precession rate or period in the source rest frame, the timescales $t_{ej} - t_{ref}$ must be in each case corrected by a factor of $1/(1 - v_x/c)$, where v_x is the line of sight velocity:

$$\frac{v_x}{c} = \beta(\sin\phi\sin(i)\cos\psi + \cos\phi\cos(i)) \quad (41)$$

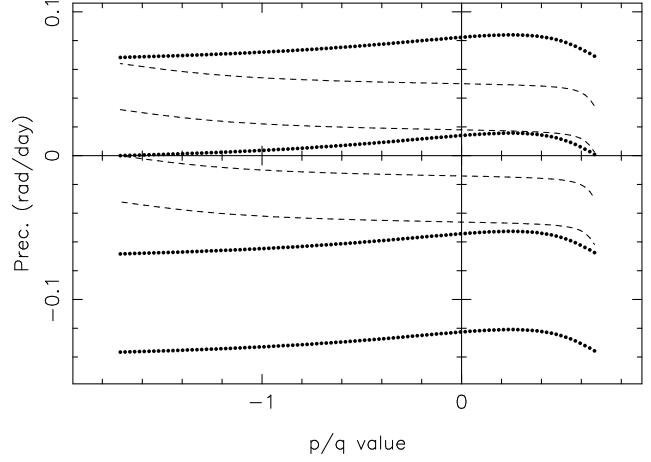


Figure 4.

Solution for the combination of the lensing quantity \tilde{p} and the rate of precession of the blazar jet (dots are used for the microarcsecond scale solution, and dashed lines for the milliarcsecond scale solution). All four possible branches are evaluated for each solution. The coincidence of the milliarcsecond scale and the microarcsecond scale solution is the desired result ($p/q=0.3$, precession rate = 0.016 rad/day). For $p/q < -1.7$ and $p/q > 0.7$, the NE image becomes negative parity, which is known to be incorrect. Positive values of the precession rate are for anticlockwise rotation in the source (as also for the NE image; parity differences cause an opposite rotation in the SW image).

With $i = 8^\circ$, $\phi = 5^\circ$, $\chi = 60^\circ$ and $\beta = 0.99$, the precession period in the source frame is 21 years. A choice of $i = 4.^\circ5$ and $\phi = 3^\circ$ with χ and β as before, yields a precession period of about 25 years.

3.6 Single plasmon events on the microarcsecond scale

From Table 1 of Jin et al. (2003), the ratio of the NE to SW core image flux densities is seen to vary as a function of observational epoch (*cf.* also the crosses plotted in Fig. 5). The variation shows two apparent maxima, indicating source variability (although variations on the timescales of a couple of weeks are possible with a combination of an apparently superluminal source and microlensing by stars in the lens galaxy — *cf.* Gopal-Krishna & Subramanian 1991 — it will be post-justified that this is not the case in the present circumstance). It is tempting to model these variations in terms of the emission of synchrotron self-absorbed plasmons. Following Expression 11 of van der Laan (1966), a series of four successively emitted plasmons is considered, expanding with constant velocity, with an initial spectral maximum at 43 GHz, and electron power law index of $3/2$. Since the model is actually underconstrained by the observations, it is only attempted to seek a consistency between the two. For each image, the emission from the series of four plasmons is computed. In the case of the SW image, this curve is scaled by the NE/SW image flux density ratio $|k| = 1.161$, derived from Section 3.3, and delayed in time relative to the NE curve by the time delay of 26 days. The middle two plasmons are constrained to have an *observed* separation, in terms of time of ejection, of $(125.2 - 30.9) = 94.3$ days, as inferred from Section 3.4. It is found necessary to introduce

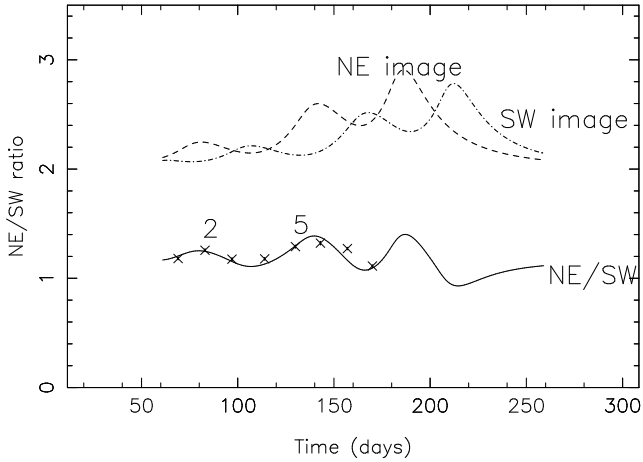


Figure 5.

(Solid curve): Simulated variation of the ratio of the NE image’s flux density to that in the SW image at 43 GHz. (Crosses): 8 epochs of data, with errors within the extent of the symbols used, from Jin et al. 2003. (Dashed line): Simulated underlying flux density variation in the NE image core, and (dash-dot line): corresponding time-delayed variation in the SW image core. Epochs 2 and 5 of the data correspond to the commencement of the observed microarcsecond-scale ‘events’ discussed in Section 3.1.

a constant core flux density, of value comparable to that of the plasmons, to simulate the data. The result of this exercise is shown in Figure 5. Note that corresponding to Epoch 2, the second plasmon has just begun to initiate a rise in the SW curve, and again at Epoch 5, the same phenomenon is observed. Hence the discontinuities in Figure 1 are seen to be a consequence of the observed appearance of a new plasmon in the SW image, as was stated in Section 3.1.

4 A MASSIVE BINARY BLACK HOLE SYSTEM FOR A CENTRAL ENGINE?

A popular model for Active Galactic Nuclei (AGNs) with precessing jets is that they host at their centres massive binary black hole systems (Begelman, Blandford & Rees 1980, Roos 1988, Roos, Kaastra & Hummel 1993, Villata et al. 1998, Villata & Raiteri 1999, Romero et al. 2000, Romero, Fan & Nuza 2003, Rieger 2004, Maness et al. 2004). The system under study in the present paper lends itself to such a possibility. The precession period intrinsic to PKS1830-211 has been derived from Section 3.5 to be about 30.8 years; as was the case for 1928+738 (with a jet precession period of 2.9 years; Roos et al. 1993) and 3C 273 (with an observed jet precession period of 16 years; Romero et al. 2000), this is too rapid to be due to geodetic precession of the jet-emitting black hole (Begelman, Blandford & Rees 1980), without suggesting a lifetime ($\sim 10^3$ years) for gravitational collapse of the binary system that is too short. One may infer, however, that the precession period is actually a result of the orbital motion of the black hole binary (as did Roos et al. 1993). In this case, the jet velocity is modulated by the orbital motion of the jet-emitting black hole. If P is the precession period, G the gravitational constant, and m and M the masses of the two black holes, then, with r as their separation from each other:

$$r^3 = \frac{P^2}{4\pi^2} G(m + M) \quad (42)$$

For a precession period in units of 30.8 years, and scaling the masses by $10^8 M_\odot$ and the separation by 10^{16} cm,

$$r_{16} = 6.833(P_{30.8})^{2/3}(m_8 + M_8)^{1/3} \text{ cm} \quad (43)$$

The gravitational lifetime of the system is given by:

$$t_{grav} = 2.9 \times 10^5 \frac{\frac{M_8}{m_8} r_{16}^4}{(1 + \frac{m_8}{M_8}) M_8^3} \text{ yrs} \quad (44)$$

In this case, using Equation 43, the lifetime of the system until gravitational collapse is:

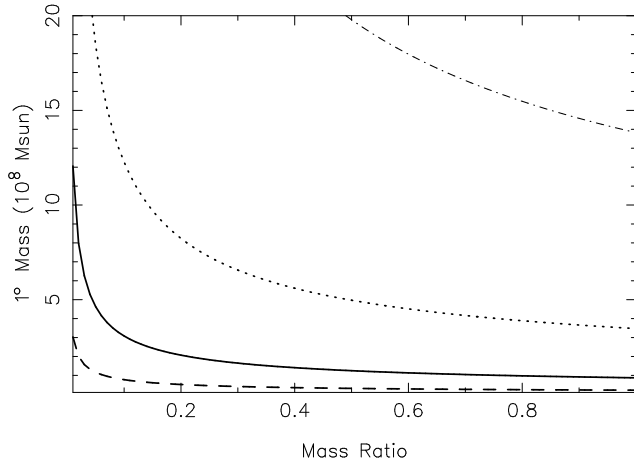
$$t_{grav} = 6.322 \times 10^8 \frac{(M_8 + m_8)^{1/3}}{m_8 M_8} \text{ yrs} \quad (45)$$

The motion of the core of the jet-emitting black hole, orbiting around its companion, would be on the scale of microarcseconds, undetectable in the 43 GHz observations used in this work.

5 DISCUSSION AND CONCLUSIONS

The observations of Jin et al.(2003) permit an analysis of the blazar source of PKS 1830-211 under atypical circumstances. Firstly, changes in the core of the source on scales of tens of microarcseconds could be probed because of the fact that the source is doubly imaged within a *single* VLBI field of view, and hence uncertainties in the separation of the two core images could be restricted to essentially thermal noise limits. Secondly, there is some degree of magnification due to lensing, which, while its numerical value cannot be determined without the existence of a standard candle/ruler within the source, still provides a closer look than might otherwise have been possible (a typical linear magnification factor would be about 3). Thirdly, this lensed system permits a detailed study of a very distant blazar (redshift $z_s = 2.51$). These observations, coupled with data from observed changes in the milliarcsecond scale of structure, make it possible to estimate the precession period of the relativistic jet in the blazar source in PKS1830-211. The observed period turns out to be 1.08 years, assuming the jet precession axis to be perfectly aligned with the line of sight to the source. This is one of the highest redshifts for which a blazar jet’s precession period has been actually measured. For PKS1830-211, the typically assumed mass of $\sim 10^8 M_\odot$ or less for each element of the central powering black hole system appears to pose no particular evolutionary problems at this redshift (*cf.*, e.g., Yoo & Miralda-Escudé 2004).

Estimating the mass of a possible central black hole system from a measured SED is confounded by the fact that PKS1830-211 is seen through the Galactic plane and is subject to much obscuration in the optical. Moreover, it is lensed, so there remains the possibility of spectral changes due to different scales of the source being magnified to different extents on account of microlensing by stars in the lens galaxy. However, a method such as measuring the timescale of variability of gamma ray emission from the source can be used. Although two timetracks, one time-delayed with respect to the other by 26 days, would be observed together, the timescale of variability is expected to be typically of the order of a day or less (Liang & Liu 2003), making it

**Figure 6.**

Plots of the gravitational lifetime of PKS1830-211 as a function of primary mass in the inferred binary black hole system (ordinates, in units of 10^8 solar masses) and the mass ratio of the two black holes (abscissae). The plots are for gravitational lifetimes of (*from top down*) 10^7 , 10^8 , 10^9 & 10^{10} years respectively. These plots use the derived intrinsic period of precession of 30.8 years; this assumes a jet bulk velocity of 0.99c.

unnecessary to correct for the time delayed track. Then, following the analysis of Liang & Liu (2003), an upper limit to the mass of the jet-emitting black hole can be derived. (Note that these authors do in fact list a black hole mass of $10^{9.2} M_{\odot}$ and a calculated minimum variability timescale of $10^{4.5}$ s in Table 1 of their paper, for the system 1830-210, based on an incorrect source redshift of 1 and the observed EGRET gamma ray flux, which would need to be corrected for lensing; the absolute magnification factor is an unknown. If it is taken as a typical value of 10, one obtains a black hole mass of $10^{8.7} M_{\odot}$ for the source at the observed redshift of 2.51; note also that this mass is determined under the assumption that the gamma ray flux is isotropic or unbeamed. This mass corresponds to a gravitational lifetime of the binary black hole system of order 10^8 years (*cf.* Figure 6)).

In passing, we note that it has been assumed in the present work that the plasmons follow straight line paths along the surface of the cone formed by the jet's precessing nozzle (following from ballistic ejection of plasmons). On the milliarsecond scale, the essentially two epochs' worth of data on the source represented by the single observation of 14 July 1996 (Garrett et al. 1997), which has been used here, permits no investigation of a possible curvature in plasmon motion. Multiepoch radio VLBI studies at, say, 43 GHz, during an active phase for the system, should be able to shed some light on the question of whether we are really seeing ballistically ejected plasmons, or whether the helical appearance of the jet is accompanied by motion of the observed features along helical paths, in which case by the time the jet has reached milliarsecond scales, observational evidence of curvature in the motion of some features might be expected. More sensitive than the observed motions of individual features perhaps would be information from the observed light curves in each image. Features moving along helical paths would show variable relativistic beaming if the jet axis is even slightly inclined to the line of sight (*cf.*, e.g., Schramm et al. 1993), exhibiting a quasi-periodicity in the

Table 1.

Data from the observations of 14 July 1996 (Garrett et al.1998)

Feature	Flux Density (mJy)	Position w.r.t. core image ($\Delta\Phi_{\alpha,A}$ or B , $\Delta\Phi_{\delta,A}$ or B)(mas)
A1 (core)	191.7 ± 1.4	(0.000, 0.000)
A2	58.9 ± 1.5	(-0.269 ± 0.002 , 0.299 ± 0.002)
A3	8.9 ± 1.4	(0.154 \pm 0.013, 0.663 \pm 0.012)
A4 (knot)	36.4 ± 1.4	(0.980 \pm 0.003, -0.150 ± 0.003)
A5	19.7 ± 1.5	(1.336 \pm 0.007, -0.334 ± 0.007)
A6	11.6 ± 2.6	(-0.582 ± 0.033 , -1.502 ± 0.038)
B1 (core)	189.2 ± 1.6	(0.000, 0.000)
B2	19.5 ± 1.5	(0.279 \pm 0.005, -0.079 ± 0.006)
B3	24.1 ± 2.4	(-0.266 ± 0.012 , 1.008 \pm 0.016)
B4 (knot)	18.7 ± 1.4	(-0.319 ± 0.005 , 0.655 \pm 0.005)
B5	43.6 ± 3.1	(-0.536 ± 0.015 , 0.352 \pm 0.009)
B6	16.4 ± 1.5	(-0.159 ± 0.007 , -0.344 ± 0.007)

intensity of emission. (Note, however, that the strict linearity apparent in Figure 1 spanning three and four epochs is a more reliable indication that on the scale of tens of microarcseconds at least, the motion of the plasmons in the present study show linear velocities, with little sign of curvature).

Lastly, there is a question regarding the plasmon lifetimes. Are the plasmons we 'see' in Jin et al. (2003) on the scale of tens of microarcseconds likely to be the progenitors of features such as have been seen on the scale of milliarseconds in Garrett et al. (1998)? We think this is unlikely; longer-lived plasmons would not permit a simple analysis such as has been possible in this work, with almost single plasmon events to be observed on the scale of tens of microarcseconds. It would appear that the plasmon emission mechanism is of a highly variable nature, only occasionally producing long-lived plasmons such as were seen in Garrett et al. (1998), but for most part producing relatively short-lived plasmons in a quiescent phase.

6 ACKNOWLEDGEMENTS

SN wishes to acknowledge Dipankar Bhattacharya and Shiv Sethi for being reliable sounding boards, especially with regard to numerical methods, and Vivek Dhawan for raising a couple of critical questions. We thank an anonymous referee for helpful comments on this work, which led to improvements.

7 APPENDIX: THE MIXED ADJUSTMENT MODEL

From Section 3.2, the five constraint equations **F**, Equations 18, 19 and the three implicit in equation 21, link the four unknowns, the transformation matrix elements T_i ($i = 1...4$) (constituting vector **X** in the present analysis), with sixteen observational quantities (positional separations, from their respective core images, of the eight features A4(B4), A2(B2), A5(B5) and A6(B6), as seen in both the NE and the SW images. These sixteen quantities constitute the vector **L** in this section. The positions of the observational features, with errors of fit, are listed in Table 1. The five equations **F** overdetermine the quantities in **X**, hence

a numerical method, the Mixed Adjustment Model, is employed to solve for \mathbf{X} . Note that the observations and the unknowns are implicitly related. The treatment here follows that described in A.Leick (1995), Section 4.4.

Let in the course of the application of this method, the 16 adjusted observations be denoted by \mathbf{L}_a , and the adjusted vector of unknowns be denoted by \mathbf{X}_a . The mathematical model is then:

$$\mathbf{F}(\mathbf{L}_a, \mathbf{X}_a) = 0 \quad (46)$$

Let \mathbf{X}_0 be a set of known but approximate values of \mathbf{X} , and denote the vector of observations by \mathbf{L}_b . Then Equation 46 may be written as:

$$\mathbf{F}(\mathbf{L}_b + \mathbf{V}, \mathbf{X}_0 + \mathbf{X}) = 0, \quad (47)$$

where \mathbf{V} and \mathbf{X} are the residuals at each stage of iteration. This essentially nonlinear form is linearized about the point $(\mathbf{L}_b, \mathbf{X}_0)$:

$${}_5\mathbf{B}_{16 \ 16} \mathbf{V}_1 + {}_5\mathbf{A}_{4 \ 4} \mathbf{X}_1 + {}_5\mathbf{W}_1 = 0, \quad (48)$$

where:

$${}_5\mathbf{B}_{16} = \left. \frac{\partial \mathbf{F}}{\partial \mathbf{L}} \right|_{(\mathbf{x}_0, \mathbf{L}_b)} \quad (49)$$

$${}_5\mathbf{A}_4 = \left. \frac{\partial \mathbf{F}}{\partial \mathbf{X}} \right|_{(\mathbf{x}_0, \mathbf{L}_b)} \quad (50)$$

$${}_5\mathbf{W}_1 = \mathbf{F}(\mathbf{L}_b, \mathbf{X}_0) \quad (51)$$

Now a least-squares estimate of \mathbf{X} is sought, with the target function $\mathbf{V}^T \mathbf{P} \mathbf{V}$, where \mathbf{P} is the 16×16 weight matrix constructed from the covariance matrix of the observations, $\sigma_o^2 \Sigma_{\mathbf{L}_b}^{-1}$, where σ_o^2 is the *a priori* variance of unit weight. The target function is minimized subject to the constraints imposed by the linearized mathematical model, Equation 48, with a vector of Lagrangian multipliers, \mathbf{K} . Hence, one minimizes with respect to \mathbf{V} , \mathbf{K} and \mathbf{X} , the function:

$$\phi(\mathbf{V}, \mathbf{K}, \mathbf{X}) = \mathbf{V}^T \mathbf{P} \mathbf{V} - 2\mathbf{K}^T (\mathbf{B} \mathbf{V} + \mathbf{A} \mathbf{X} + \mathbf{W}), \quad (52)$$

and the three constraint equations arising from this process are used to calculate \mathbf{V} , \mathbf{K} and \mathbf{X} . Since the actual mathematical model is non-linear, it is necessary to iterate to a solution the actual values of \mathbf{V} , \mathbf{K} and \mathbf{X} . The iterative process is said to converge if:

$$|(\mathbf{V}^T \mathbf{P} \mathbf{V})_i - (\mathbf{V}^T \mathbf{P} \mathbf{V})_{(i-1)}| < \epsilon, \quad (53)$$

where ϵ is a small positive number (here taken as 10^{-8}). In the present case, the calculation converged in five iterations, with a final value of $\mathbf{V}^T \mathbf{P} \mathbf{V} = 9$. The estimated *a posteriori* variance of unit weight, σ_o^2 , is therefore $\mathbf{V}^T \mathbf{P} \mathbf{V} / (5-4) = 9$.

REFERENCES

Begelman, M.C., Blandford, R.D., Rees, M.J., 1980, *Nature*, 287, 307
 Carilli, C.L., Menten, K.M., Reid, M.J., Rupen, M., Claussen, M., 1998, *ASPC*, 144, 317
 Chengalur, J.N., de Bruyn, A.G., Narasimha, D., 1999, *A&A*, 343, 79
 Courbin, F., Lidman, C., Frye, B.L., Magain, P., Broadhurst, T.J., Pahre, M.A., Djorgovski, S.G., 1998, *ApJ*, 499, 119
 Courbin, F., Meylan, G., Kneib, J.-P. & Lidman, C., 2002, *ApJ*, 575, 95
 Dondi, L., Ghisellini, G., 1995, *MNRAS*, 273, 583

Frye, B.L., Courbin, F., Broadhurst, T.J., Welch, W.J.W., Lidman, C., Magain, P., Pahre, M. & Djorgovski, S.G., 1999, *ASPC*, 156, 240
 Garrett, M. A., Nair, S., Porcas, R. W., Patnaik, A. R., 1997, *Vistas in Astronomy*, 41, 281
 Garrett, M. A., Leppanen, K., Porcas, R. W., Patnaik, A. R., Nair, S., Teraesranta, H., 1998, *ASPC*, 114, 313
 Gopal-Krishna & Subramanian, K., 1991, *Nature*, 349, 766
 Gower, A.C., Gregory, P.C., Unruh, W.G., Hutchings, J.B., 1982, *ApJ*, 262, 478
 Guirado, J.C., Jones, D.L., Lara, L., Marcaide, J.M., Preston, R.A., Rao, A.P., Sherwood, W. A., 1999, *A&A*, 346, 392
 Hagiwara, Y., Fujisawa, K., Edwards, P., Hirabayashi, H., Murata, Y., Kobayashi, H., Iwata, T., IAUS, 173, 341
 Hjellming, R.M. & Johnston, K.J., 1981, *ApJ*, 246, 141
 Jin, C., Garrett, M. A., Nair, S., Porcas, R. W., Patnaik, A. R., Nan, R., 2003, *MNRAS*, 340, 130
 Jones, D.L., Preston, R.A., Murphy, D.W., Jauncey, D.L., Reynolds, J.E., Tzoumis, A.K., King, E.A., McCulloch, P.M., Lovell, J.E.J., Costa, M.E., van Ommen, T.D., 1996, *ApJ*, 470, 23.
 Kochanek, C.S. & Narayan, R., 1992, *ApJ*, 401, 461
 Lehar, J., Falco, E.E., Kochanek, C.S., McLeod, B.A., Muñoz, J.A., Impey, C.D., Rix, H.-W., Keeton, C.R. & Peng, C.Y., 2000, *ApJ*, 536, 584
 Liang, E.W. & Liu, H.T., 2003, *MNRAS*, 340, 632
 Lidman, C., Courbin, F., Meylan, G., Broadhurst, T., Frye, B., Welch, W.J.W., 1999, *ApJ*, 514, 57
 Leick, A., 1995, *GPS Satellite Surveying*, Second Edition, John Wiley & Sons, Inc.
 Lovell, J.E.J., Reynolds, J.E., Jauncey, D.L., Backus, P.R., McCulloch, P.M., Sinclair, M.W., Wilson, W.E., Tzioumis, A.K., King, E.A., Gough, R.G. & 4 coauthors, 1996, *ApJ*, 472, 5L
 Lovell, J.E.J., Jauncey, D.L., Reynolds, J.E., Wieringa, M.H., King, E.A., Tzoumis, A.K., McCulloch, P.M. & Edwards, P.G., 1998, *ApJ*, 508, 51.
 Maness, H.L., Taylor, G.B., Zavala, R.T., Peck A.B. & Pollack, L.K., *ApJ*, 602, 123 (2004)
 Mathur, S. & Nair, S., 1997, *ApJ*, 484, 140
 Mattox, J.R., Schachter, J., Molnar, L., Hartman, R.C. & Patnaik, A.R., 1997, *ApJ*, 481, 95
 Nair, S., Narasimha, D. & Rao, A.P., 1993, *ApJ*, 407, 46
 Oshima, T., Mitsuda, K., Ota, N., Yonehara, A., Hattori, M., Mihara, T., & Sekimoto, Y., 2001, *ApJ*, 551, 929
 Rao, A. P., & Subrahmanyan, R., 1988, *MNRAS*, 231, 229
 Rieger, F.M., 2004, *ApJ*, 615, L5
 Romero, G.E., Benaglia, P. & Combi, J.A., 1997, *A&AS*, 124, 307
 Romero, G.E., Chajet, L., Abraham, Z. & Fan, J.H., 2000, *A&A*, 360, p. 57
 Romero, G.E., Fan, J.-H. & Nuza, S.E., 2003, *ChJAA*, 3, 513
 Roos, N., 1988, *ApJ*, 334, 95
 Roos, N., Kaastra, J.S. & Hummel, C.A., 1993, *ApJ*, 409, 130
 Schramm, K.-J., Borgeest, U., Camenzind, M., Wagner, S.J., Bade, N. et al., 1993, *A&A*, 278, 391
 Subrahmanyan, R., Narasimha, D., Rao, A.P. & Swarup, G., 1990, *MNRAS*, 246, 263
 van der Laan, H., 1966, *Nature*, 211, 1131
 van Ommen, T.D., Jones, D.L., Preston, R.A. & Jauncey, D.L., 1995, *ApJ*, 444, 561
 Villata, M. Raiteri, C.M., Sillanpaa, A. & Takalo, L.O., 1998, *MNRAS*, 293, L13
 Villata, M. & Raiteri, C.M., 1999, *A&A*, 347, 30
 Wiklind, T. & Combes, F., 1996, *Nature*, 379, 139
 Wiklind, T. & Combes, F., 1998, *ApJ*, 500, 129
 Winn, J.N., Kochanek, C.S., McLeod, B.A., Falco, E.E., Impey, C.D., Rix, H.-W., 2002, *ApJ*, 575, 103
 Yoo, J. & Miralda-Escudé, J., 2004, *ApJ*, 614, L25